Reduced Graphene Oxide Aerogels with Controlled Continuous Microchannels for Environmental Remediation

Vanesa Rodríguez-Mata, José Miguel Gonzalez-Dominguez, Ana M. Benito, Wolfgang K. Maser, Enrique García-Bordejé∗

Instituto de Carboquímica (ICB-CSIC), Miguel Luesma Castán 4, 50018 Zaragoza, Spain, jegarcia@icb.csic.es

Abstract

3D porous graphene microarchitectures with aligned and continuous channels are of paramount interest for several applications such as pollutant removal, energy storage or biomedical engineering. For these applications, an accurate control in the pore microstructure is of capital importance. Freeze casting is a well-stablished technique to prepare graphene aerogels with unidirectional channels. This technique is typically applied to plain GO colloids, leading to discontinuous microchannels. Herein we have carried out the freeze process starting directly with partially reduced graphene (rGO) hydrogels prepared by a prior hydrothermal treatment in autoclave. This approach leads to the formation of aerogels with aligned and continuous microchannels, enabled by an

∗ Corresponding author: Tel.:+ 34 976733977; fax.: +34 976733318 *E-mail address:* jegarcia@icb.csic.es

intermediate crosslinking degree of the rGO nanosheets, carefully controlled by keeping the time of the prior hydrothermal process between the thresholds of 45-75 minutes. To the best of our knowledge, the effect of the degree of crosslinking in the freeze casting process is not reported.. The resulting rGO aerogels with highly aligned microchannel structure reveal superior properties over its isotropic counterpart of randomly oriented pores for the absorption of non-polar solvents and the selective adsorption of an aromatic compound dissolved in an alkane. Our combined hydrothermal-freeze casting approach thus affords aligned microchannel rGO aerogels of enormous potential for environmental remediation.

1. Introduction

Graphene has many outstanding properties such as high electrical and thermal conductivities, strength, flexibility etc. In the past years tremendous efforts have been made to fabricate graphene-based 3-D bulk materials. However, the *a priori* excellent properties of graphene are hardly transferred to their assemblies due to graphene sheets stacking. 3-D graphene networks with an open structure have gained a tremendous interest due to their excellent properties such as high surface to volume ratio, extremely lightweight,[1] favourable absorption properties,[2-3] compressibility,[1-2, 4-5] high thermal and electrical conductivities,[6-8] and mechanical properties.[9] Moreover, the high surface area of 3D graphene porous solids made them ideal candidates as scaffold to support other nanomaterials,[10-24] doping[17, 25-28] or forming hybrids[11, 20, 29-31] for different applications such as catalysis, supercapacitors, batteries, selective absorption, sensor, biomedicine or composite materials. The preparation of 3-D porous superstructures based on graphene building blocks has been carried out by different techniques such as the gelation of GO dispersions,[32] emulsion templating[33] or chemical vapour deposition on a sacrificial

template.[34] The sol-gel approach starting from GO is a very cost-effective and versatile method which can also benefit from the rich surface chemistry of GO[35-37] for doping or forming hybrids.[38] Moreover, this method allows moulding the macroscopic shape to that of the container. Other techniques such as wet spinning[8], electrospinning[39] or 3-D printing[40] of GO dispersions have been also used to prepare aerogels with specific macroscopic morphologies. All the above-mentioned methods usually lead to a foam-like superstructure with randomly oriented pores. Nevertheless, materials with aligned microstructures are interesting for many applications such as energy storage, filtration, microfluidics, nanocomposites and tissue engineering, among others.[41-43] The anisotropic orientation of graphene sheets has high impact on the conductive percolation in composites,[44] the transport of fluids and particle suspensions and the growth of active matters.[45] In this context, aerogels with anisotropic channels are excellent candidates for environmental remediation such as the cleaning of oil spills or the water decontamination from organic pollutant, where foam like aerogels performed extraordinarily well.[2, 46-47]

A widely used approach to create 3D superstructures of oriented pores from different materials is unidirectional freeze casting, also called ice-segregation-induced self-assembly (ISISA) process.[48-49] It has been successfully applied to gelatin [50], ceramics,[51] carbon nanotubes,[52-53] and different composites of graphene and polymers.[13] This technique relies on the growth of straight ice crystal bars by unidirectional freezing. Some researchers have performed the unidirectional freezing of graphene[54] or GO suspensions.[44, 55] Starting from stabilized suspensions of graphene flakes, a linker such as a polymer is usually required to preserve the 3D structure.[54] On the other hand, aerogels synthetized by unidirectional freeze drying starting from GO suspensions[44, 55-60] exhibited an orientation of the graphene nanosheets rather than continuous

microchannels. This occurs because nanosheets are very well dispersed in a water matrix and often lack sufficient binding strength among them to create a well-connected network. The continuity of the channel walls in aerogel is beneficial to increase the electrical conductivity in composites or to fill the channels with a fluid since the aligned pores should exert lower back pressure compared to randomly oriented. Adding to GO a crosslinking agent[61] or an alcohol as antifreezing agent[62] lead to well aligned microchannels upon unidirectional freezing but with graphene bridges perpendicular channels walls. There are only few recent reports of continuous microchannels and they use a mild reductant (ascorbic acid) and heat treatment.[63-66] Accordingly, it is apparent that a certain degree of GO reduction is beneficial to attain continuous microchannels by freeze casting. Despite all this plethora of literature leading to different microstructures upon freeze casting, to our knowledge there is no a systematic study trying to generalize how the extent of reduction/gelation affects the formation of the microchannels.To the best of our knowledge, while hydrothermal reduction in autoclave has been widely used for the formation of foam-like graphene aerogels,[46, 67-68] the freeze casting starting from graphene hydrogels prepared by hydrothermal reduction in autoclave has not been reported yet.

Here we use a linker-free approach leading to aerogels with continuous and aligned microchannels. In contrast to the common practice of freeze casting of GO dispersion, our novel approach uses reduced GO (rGO) hydrogels for freeze casting. The rGO hydrogels are prepared by hydrothermal reduction of GO dispersions in an autoclave. Likewise, the rGO nanosheets within the hydrogel are partially crosslinked by π-π interactions and H-bonds, which are inexistent in pristine GO dispersions. rGO hydrogels with different degree of crosslinking have been prepared by varying the hydrothermal treatment times. This enabled to disclose the impact of the crosslinking

degree on the formation of aligned and continuous microchannels. Finally, aerogels with unidirectional pores and random pores have been compared for the absorption of non-polar solvents and for the selective adsorption of an aromatic compound *vs.* alkane in a continuous operation mode.

2. Experimental section

The different steps for the preparation of the reduced graphene oxide aerogel are illustrated in Scheme 1. The starting GO is a commercial 4 mg/ml dispersion of Graphenea Co. (San Sebastián, Spain, Ref. **GO-4-1000**). The characterisation of graphene flakes is shown in Figure S1 of supporting information. To carry out the hydrothermal treatment, 10 ml of a 2 mg/mL GO aqueous dispersions was introduced in a Teflon-lined autoclave. The liquid to autoclave volume ratio is 0.22. The autoclave is introduced in an oven at 180 ºC, reaching a pressure of 10 Bar and kept for a certain time (ranging from 45 min to 18 h). Subsequently, the autoclave is withdrawn from the oven and left to cool down at ambient conditions. Likewise, the rate of cooling down is comparable for all the preparations. When the autoclave is at room temperature, it is opened and a monolithic hydrogel has been formed which takes the shape of the container inside the autoclave.
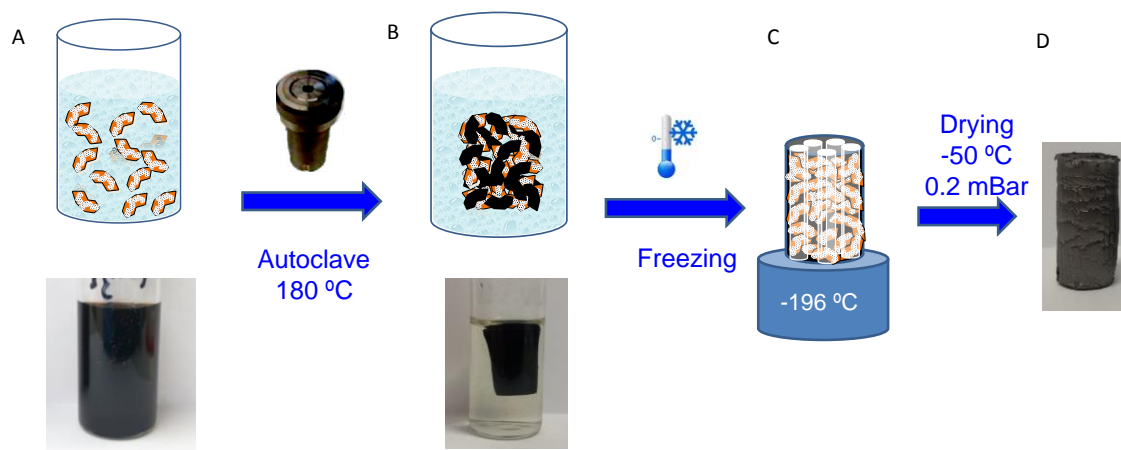
Scheme 1. Steps for the synthesis of reduced graphene oxide (rGO) aerogels. A) GO dispersion; B) hydrogel formed by reduced GO nanoplatelets; C) cryogel by unidirectional freezing at -196 ºC; D) rGO aerogel

The hydrogel attained was then frozen using two different approaches. In the so-called "bulk freezing (B)", the vial containing the hydrogel was fully immersed in liquid nitrogen (-196 ºC). The other approach is the so-called "unidirectional freezing (U)". In this approach, a vial of aluminium bottom and glass walls containing the hydrogel is thermally insulated by Styrofoam except the aluminium bottom. The aluminium bottom is placed onto a 5 cm diameter metal platform which is externally cooled by liquid N_2. This creates a uniaxial thermal gradient and the hydrogel is cooled from the bottom to the top. The solidified hydrogel attained either by "bulk freezing" or "unidirectional freezing" is then transferred into a freeze-drying vessel (Telstar Cryodos) under vacuum (less than 0.3 mbar) and freeze-dried at around 223 K for 48 h to obtain the aerogel. The aerogels are denoted as GAX_Y, where X is the time of hydrothermal treatment and Y is the freezing method, either "B" for bulk freezing or "U" for unidirectional freezing.

The density of the cylindrical aerogel (ρ_c) in g cm^{-3} was calculated as weight (w) of the cylinder divided by the volume (V_c), which was calculated as:

$$V_c = \pi \frac{D^2}{4} L \qquad \text{eq. 1}$$

The diameter of cylinder (D) and the length of cylinder (L) in cm were measured with a micrometer gauge.

The total pore volume (Vp) was calculated as

$$Vp = V_c - \frac{w}{\rho_g} \qquad \text{eq. 2}$$

were w is the weight of the cylinder and ρ_g is the density of rGO nanosheets which was assumed to be 1.06 g cm^{-3}, as reported for graphene.[69]

Surface areas were determined by N_2 adsorption at 77 K (BET) using a Micromeritics ASAP 2020 apparatus, after outgassing for 4 h at 423 K. Alternatively, it was also determined by CO_2 adsorption (Dubinin–Radushkevich) at 273 K up to 1 Bar in the same apparatus, after outgassing under the same conditions.

Raman characterisation was performed on a Horiba Jobin Yvon, LabRAM HR UV-VIS NIR. Raman spectra were recorded with an Ar-ion laser beam at an exciting radiation wavelength of 532 nm. The subtraction of the baseline and the fitting of the peaks were performed with Originpro 8.5 software.

SEM analysis was carried out with a microscope SEM EDX Hitachi S-3400 N with variable pressure up to 270 Pa and with an analyzer EDX Röntec XFlash de Si(Li). The images were obtained both from the secondary and backscattered signal.

X-ray diffraction (XRD) patterns were recorded using a Bruker D8 Advance diffractometer in configuration theta-theta using nickel-filtered CuK α radiation (wave length=1.54 Å), a graphite monochromatic source and scintillation detector. 2Θ angles from 3 to 80 º were scanned with a length step of 0.05 and an accumulation time of 3 s.

The X-ray photoelectron spectroscopy (XPS) was carried out with an ESCAPlus Omnicrom equipped with a Mg Kα radiation source to excite the sample. Calibration of the instrument was performed with Ag $3d_{5/2}$ line at 368.27eV. All measurements were performed under ultra-high vacuum, beyond 10^{-10} Torr. Internal referencing of spectrometer energies was made using the C 1s signal at 284.6 eV. The curve fitting of the spectra was performed using CASA XPS software The XPS peaks were fitted to GL(70) lineshape (a combination of 30% Gaussian and 70% Lorentzian character), performing a Shirley background subtraction. In the fitting procedure the FWHM (full width at half maximum) values were fixed at a maximum limit of 2 eV.

The oxygen elemental analysis is carried out directly in a Flash 1112 de Thermofisher. The sample in platinum capsules is pyrolised at 1070 ºC under He flow. The produced gases flow through a reducing bed of carbon black that transforms all COx to CO. Subsequently the gases flow through a polar chromatographic column that separates CH_4 from CO and the latter is detected and quantified with a thermal conductivity detector calibrated with sulphanilamide.

Direct current (DC) electrical conductivity was measured with a Keithley 4200-SCS source measurement unit. The samples were placed between two copper sheets pressed mildly to both ends of the aerogel by a wood press. Measurements were carried out in a two-probe configuration, with each copper sheet working as an electrode. In a typical measurement, the intensity was registered varying the voltage between -200 and 200 mV. The resistance was calculated from the slope of the line.

The experiments of hexane absorption were carried out by introducing the aerogel in a beaker with the organic liquid. It was kept for 5 minutes that it is more than enough time to completely fill the porosity of aerogel, which was corroborated because the aerogel sinks to the bottom in the organic liquid and there is not more gas bubbles emerging. After 5 minutes, the aerogel is withdrawn from the liquid with pincers and the excess liquid in the external surface is dried carefully with a cellulose paper. Immediately, the aerogel weight was measured in a precision balance. the process of withdrawing the sample from hexane and weighting was carried out very fast (5 seconds) in order to avoid any evaporation. The difference between the weight of the pristine aerogel and the aerogel after absorption of the organic is the liquid absorbed.

The setup for the adsorption experiments in flow is displayed in Figure S2. In the experiment, the aerogel is tightly fitted inside a 10 mm internal diameter column with adjustable ends. An infusion syringe impulses 1 ml/min hexane coloured with Sudan III

dye through the aerogel in the column connected by microfluidic tubes (1/16 inch external diameter). The concentration of Sudan III at the outlet is measured with a UV-spectrophotometer (Shimadzu UV-2600) using the software UVPROBE and measuring the absorbance at 240 nm where the maximum absorbance of Sudan III occurs (Figure S3).

3. Results and discussion

Graphene hydrogels were prepared by hydrothermal treatment of GO dispersions under basic pH. Previously, we found that graphene aerogels prepared under basic pH (adding NH_3) were more deoxygenated and with higher pore volume than those prepared under acidic pH.[46] The larger porosity was partially due to the curved morphology of graphene nanosheets that prevented restacking. The concentration of initial GO dispersion was also selected in base to results of previous paper, since lower GO concentration (1 mg ml^{-1}) did not give rise to a single monolithic aerogel but several pieces, and higher concentration (4 mg ml^{-1}) produced denser aerogels. As the hydrothermal treatment proceeds, the oxygen content and the amount of entrapped water in the hydrogel decreases (Table 1). Consequently, GO nanosheets are gradually reduced to give rGO nanosheets. The oxygen content reduction and removal of water increases the amount of crosslinks by π-π interactions of hydrophobic domains,[68, 70] leading to the phase segregation of a hydrogel for treatment times longer than 45 min. The aerogels prepared for different hydrothermal treatment times were characterised by Raman. Typically, GO exhibits two main characteristic peaks: G band (around 1580 cm^{-1}) that is caused by the first order scattering of the E_{2g} phonon of sp^2 C atoms and D band (around 1345 cm^{-1}) that results from a breathing mode of the K-point phonons of A_{1g} symmetry. Close to G band is the D′ (1606–1612 cm^{-1}) corresponding disordered graphitic lattice with E_{2g}

symmetry. The D band is associated with structural defects such as dangling bonds in plane terminations of disordered graphite. The intensity ratio of the D and G bands (I_D/I_G) is usually a measure of defects in graphene[71-72]. We fitted the spectra taking into consideration de D´ band (Figure S4) and calculated the I_D/I_G ratio (Table 1). This ratio decreases initially after 30 min of hydrothermal treatment due to the extensive deoxygenation from initial GO. For further hydrothermal treatment, the ID/IG ratio increases indicating the creation of further dangling bonds, vacancies[73] or even decreasing the average size of the sp^2 domains.[74]

The hydrogel is subsequently freeze dried either upon unidirectional freezing (U) or bulk freezing (B) to give an graphene aerogel (GA). Figure 1 compares the macroscopic aspects of aerogels derived from hydrogels attained at different times of hydrothermal treatment using the two freezing methods. The geometrical aspect of the aerogel cylinders (diameter and heights) for the different synthesis conditions are shown in Figure 1 b and c, respectively .

Table 1. Elemental analysis and XPS quantification for aerogels prepared at different hydrothermal treatment times and unidirectional freeze drying

hydrothermal treatment time (min)	elemental analysis		XPS		Total pore volume^a	**Raman intensity ratios**
	O/C (at%)	N/C (at%)	O/C (at%)	N/C (at%)	cm^{3}g^{-1}	**I_D/I_G**
0	72.4	4.1	n.d.*	n.d.*	n.d.**	1.26
30	28.8	10.9	17.6	5.6	n.d.**	1.11
45	14.9	10.6	8.9	6.5	153	1.11

75	14.4	10.5	8.4	6.9	111	1.22
105	13.2	9.7	8.3	7.1	94	1.23
1080	13.0	10.3	8.0	6.3	75	1.20

* not determined because the oxygenated groups are unstable under the X-ray beam

** not determined because the hydrogel was not formed yet at that time

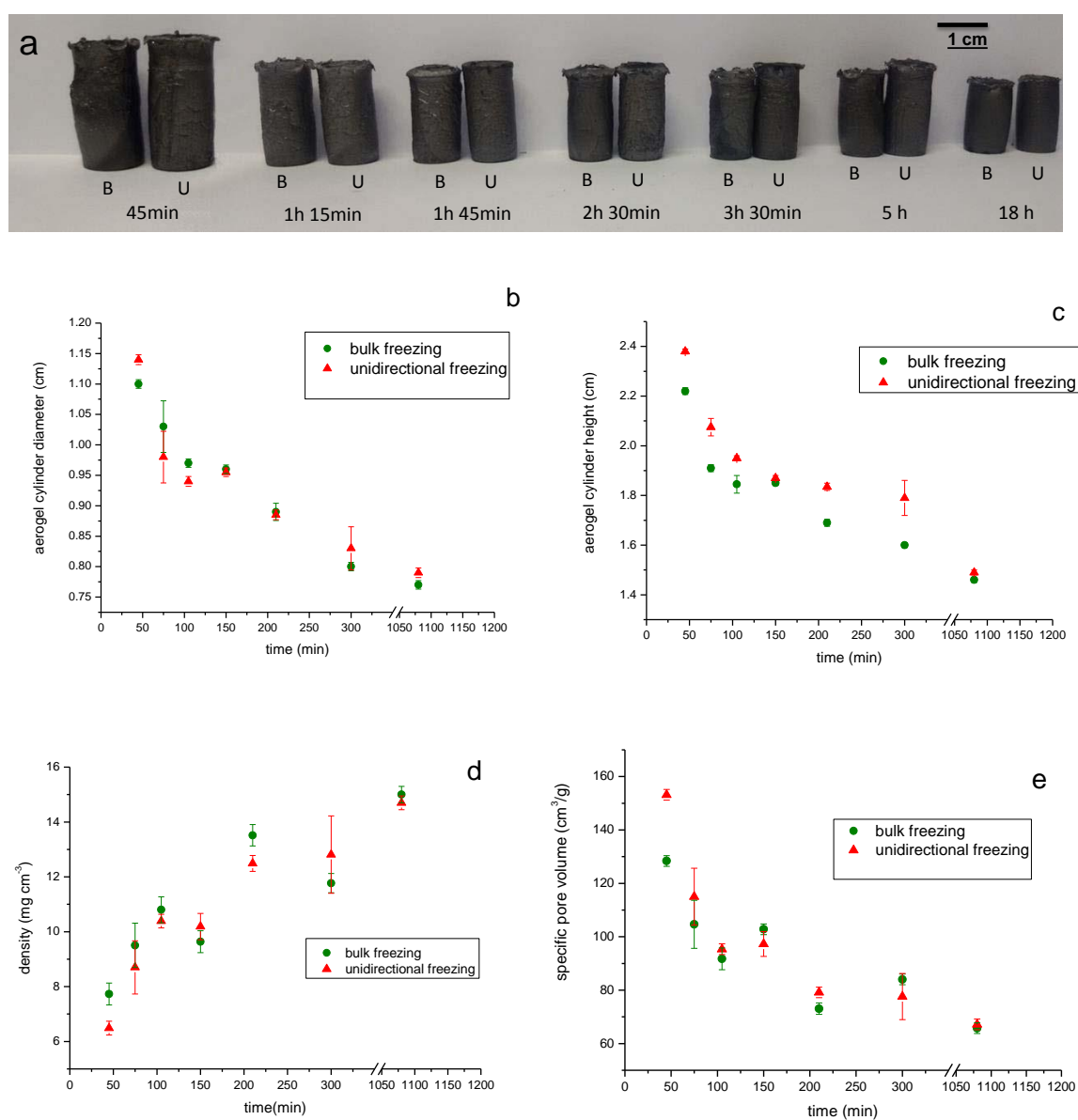[a] includes volume of macropores and it is calculated using equation 2

Figure 1. Evolution with hydrothermal treatment time of macroscopic aspects of prepared aerogels: (a) Photography of aerogels, (b) diameter, (c) height, (d)

density and (e) specific pore volume. "B" stands for bulk freezing and "U" stands for unidirectional freezing.

Both diameter and height decrease gradually as the hydrothermal treatment time increases. This is a macroscopic indication of the intensification of the crosslinking between graphene nanosheets. While the diameter varies randomly with the freezing method, the height is systematically higher for the aerogels prepared by unidirectional freezing than for their bulk frozen counterparts, pointing out that the cylinder stretches along the direction of the freezing. Taking into account these dimensions and the weight of aerogel, the density and pore volume of the aerogel were determined (Figure 1 d and e respectively). The density of aerogel rises and the specific pore volume decays as the time of hydrothermal treatment increases. For the two shortest times, unidirectional freezing provides significantly lower densities and higher specific pore volume than bulk freezing. There is a sharp change of density and pore volume between samples prepared at 45 and 75 min. 45 min is the lowest limiting time for aerogel formation because for 30 min the hydrogel is not formed. For 30 min, the rGO nanosheets remain dispersed in water because they are not sufficiently reduced and the binding to water molecules is prevalent over the binding between rGO nanosheets by π-π stacking and H-bonds.[68, 70]

Another difference between bulk and unidirectional freezing is the regularity of the cylinder shape. For 45 min of hydrothermal treatment, unidirectional freezing led to more perfect cylinders than bulk freezing. The latter exhibits some bumps at the external walls (Figure S5 of supplementary information). These bumps are generated

during the drying of the aerogel, thus apparently the unidirectional drying exert less strains in the structure.

The nanoscale texture and structure werestudied by gas physisorption and SEM. The Micro- and meso-pore volumes and Surface area determined by applying the BET method to the adsoption isotherms are displayed in table S1 of supporting material. The surface areas range between 98-180 m^2 g^{-1} and pore volumes between 0.18-0.50 cm^{3}g^{-1}. In general, these values increase with the time of hydrothermal treatment. The volume of these pore is much lower than the macropore volume that ranges 75-150 cm^{3}g^{-1} (Table 1) and decreases with the hydrothermal treatment time. The textural values do not differ significantly between aerogels prepared by bulk freezing and unidirectional freezing. Figure 2 shows representative SEM images of graphene aerogel prepared using bulk freezing (B) from hydrogels attained after different hydrothermal treatment times. Longitudinal sections of the aerogels are displayed at the left-side panels while cross sections are displayed at the right-side panels. There are not substantial differences between cross-sections and longitudinal sections. Therefore, the porosity of the sample is isotropic consisting of random pores of a foam-like aspect. The porosity of aerogel GA45min_B is different to that of the other aerogels. For GA45min_B (Figure 2a and 2b), the rGO nanosheets are apparently loose while for the rest of samples rGO nanosheets are more crosslinked. As the hydrothermal treatment time increases, the rGO nanosheets get closer and the openings become smaller, confirming the increase of the amount of crosslinks. This agrees with the increasing aerogel density and macroscopic shrinking (*vide supra*). The aerogels attained at the longest hydrothermal treatment times exhibited still a high pore volume (80 cm^{3}g^{-1}) because the basal planes of nanosheets are not stacked, mainly due their corrugated morphology [46].
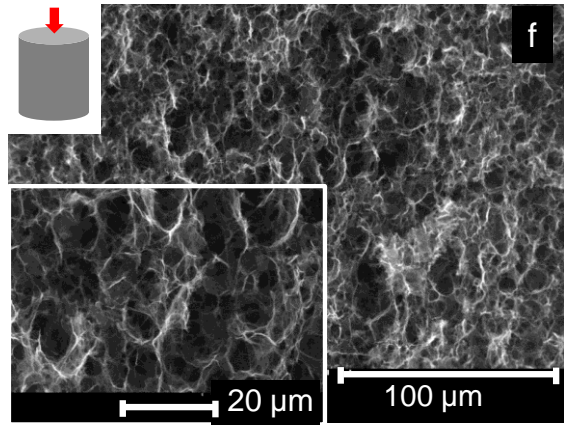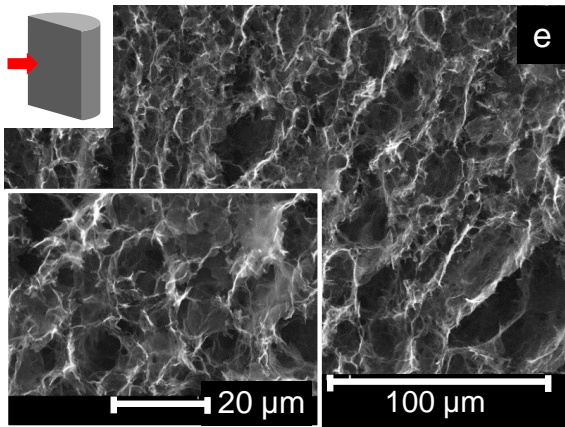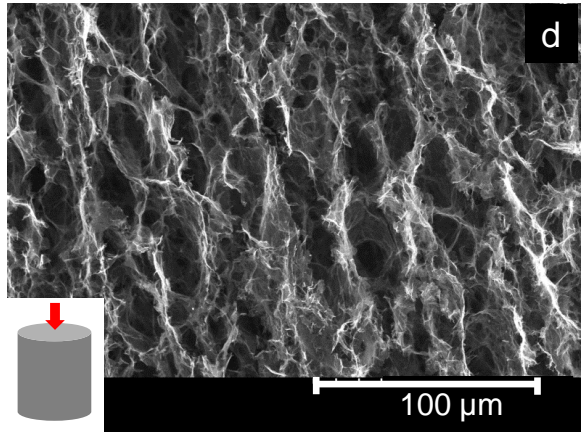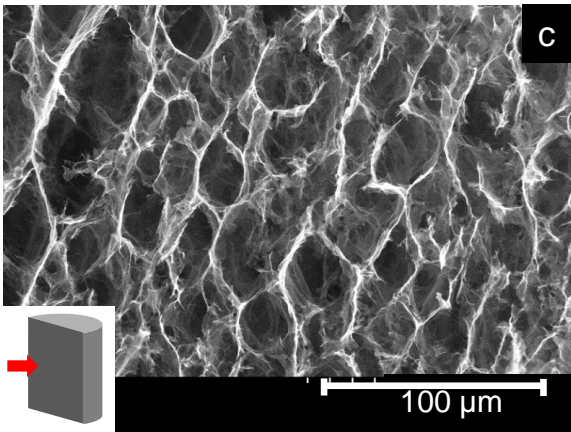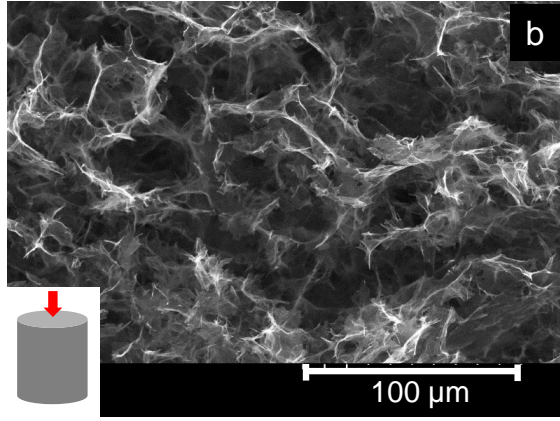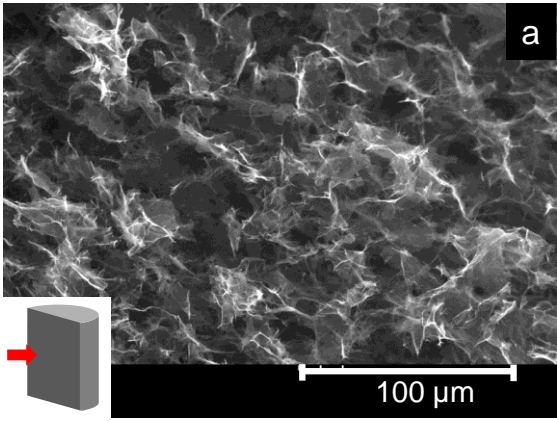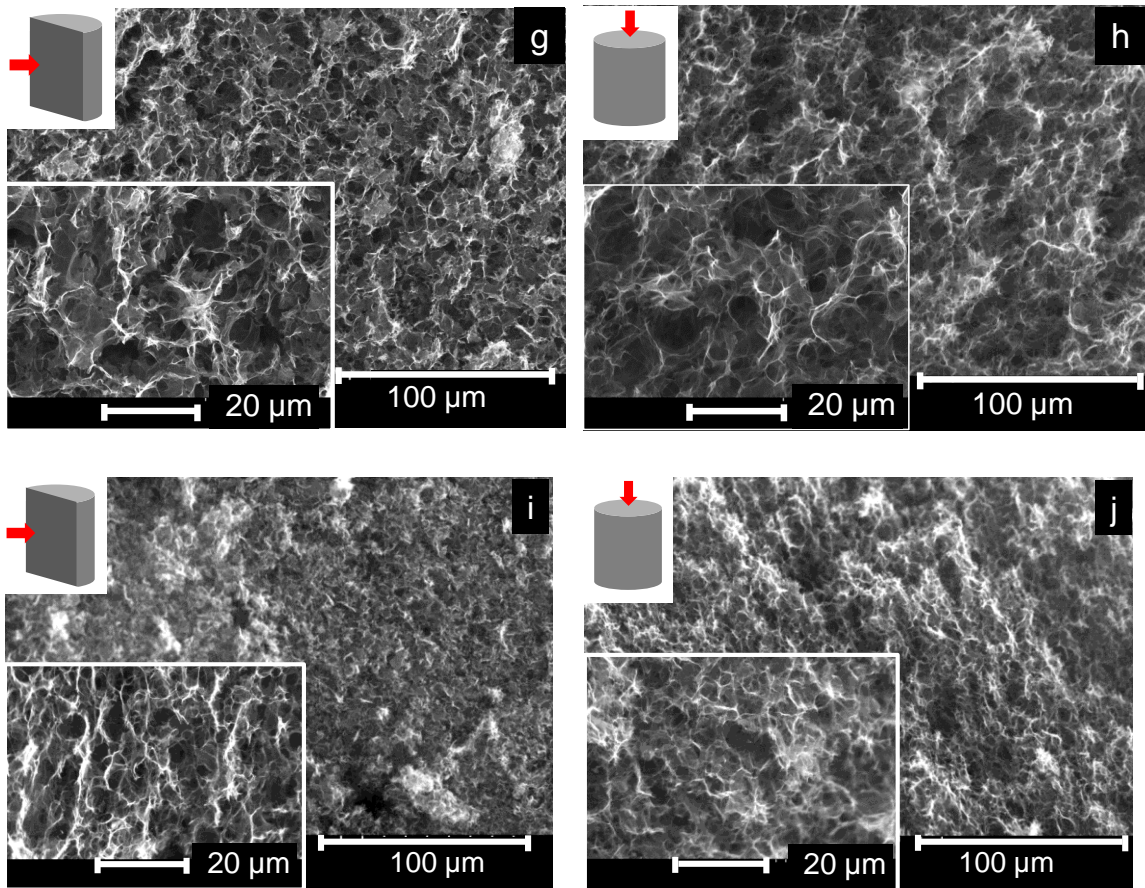
Figure 2. Representative SEM images of longitudinal sections (a,c,e,g,i) and cross sections (b,d,f,h,j) of aerogels prepared using bulk freezing of hydrogels attained at different hydrothermal times: (a,b) GA45min_B; (c,d) GA75min_B, (e,f) GA105min_B; (g,h) GA210min_B ; (i,j) GA18h_B.

The SEM images in Figure 3 are representative of aerogels fabricated using the unidirectional freezing (U) for different hydrothermal treatment times. Figure 3a and b shows SEM images of aerogels prepared by unidirectional freeze drying of 30 min hydrothermally-treated GO, *i.e.* before the formation of the hydrogel has been acomplished. Although a certain orientation of the graphene basal planes parallel to the longitudinal direction is observed, continuous microchannels are not formed, alike for the unidirectional freeze drying of GO colloids in the literature. [44, 55-58] The reason why this occurs is because the rGO nanosheets are not sufficiently close and crosslinked to

15

form a connected network. In contrast, for aerogels prepared after 45 min and 75 min hydrothermal treatment times, continuous and aligned microchannels are clearly observed oriented parallel along the height of the aerogel cylinder (Figure 3 c and e). The entire monolith exhibits a structure resembling that of a honeycomb of aligned channels with the channel rows arranged concentrically around the axis (Figure 4). This structure is templated during the freezing process, whereby straight ice crystal rods grow from the bottom, where the cooling source is located, to the top. The abundant and linked graphene nanosheets wrap around the ice bars forming a continuous network. The microchannel width ranges between 25-100 μm for both GA45min_U and GA75min_U, regardless of the hydrothermal treatment time. This pore size range is consistent with other continuous microchannels reported in the literature[64] suggesting that this outcome is determined by the size of ice-crystals. There are some minor edge effects (few microns) determined by the interfacial phenomena between hydrogel and cooling source. The microchannel diameter distribution is not completely uniform through the cross-section of the monolithic aerogel (Figure 4), the channels being narrower at the centre and at the outer layers due probably to interphase phenomena leading to a higher concentration of nanosheets both at the centre and at the interphase with the container. In contrast, the pore size is uniform along the length of the aerogel. Thus, the pores are almost the same size near the cooling plate than in the opposite end. This could be due because the ice rods grow very fast, the cylinder length is low enough, the cylinder is thermally insulated around and the temperature gradient advances at the same rate that the rod upper end.

For GA105min_U and GA210min_U the channels are not observed anymore. However, there is a certain anisotropy since the nanosheets basal planes are somehow oriented

parallel to the ice growth direction, *i.e* basal planes are predominant in a longitudinal cut (Figure 3g and 3i) and the graphene edges and openings stand out in the cross section (Figure 3 h and 3j). The opening widths range between 7 and 20 μm for GA105min_U, being <10 μm for GA210min_U. These sizes are significantly smaller than those of GA45min_U and GA75min_U. The aerogel prepared at the longest hydrothermal treatment time (18 h) is totally isotropic despite the unidirectional freeze drying. The absence of separated channels for hydrothermal treatment times equal or longer than 105 min must be due to the constrained mobility of the highly interlinked rGO nanosheets which impedes the growth of straight ice rods. In contrast, for GA45min_U and GA75min_U, the rGO nanosheets are looser and hence endowed with high freedom to move and wrap around the ice rods.

The electrical continuity of the aerogel was corroborated by measuring the electrical conduction in the axial and radial direction (Table S2). The values of conductivity are larger for a longer hydrothermal treatment time. The anisotropy in conductivity is observed for sample GA45min_U while for bulk-frozen materials and for GA105min_U, the conductivity exhibited an isotropic behaviour in agreement with SEM observations.

18
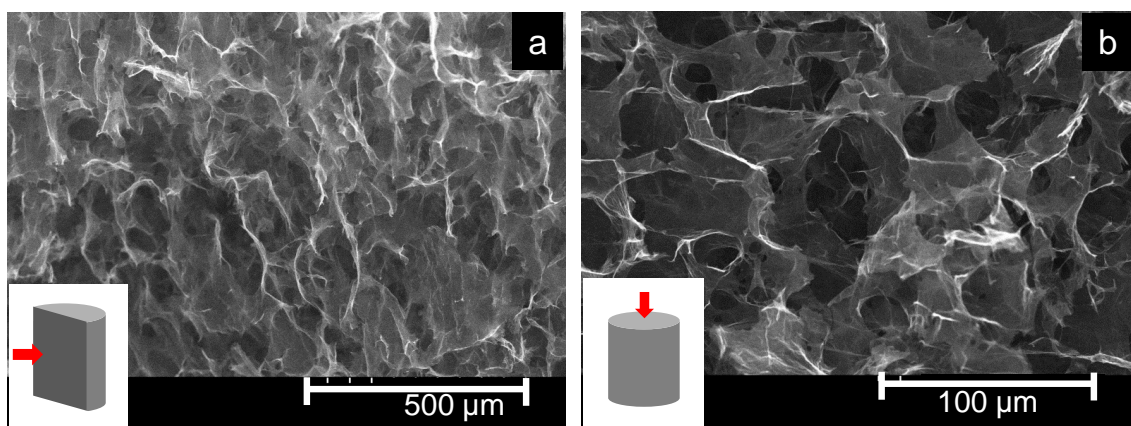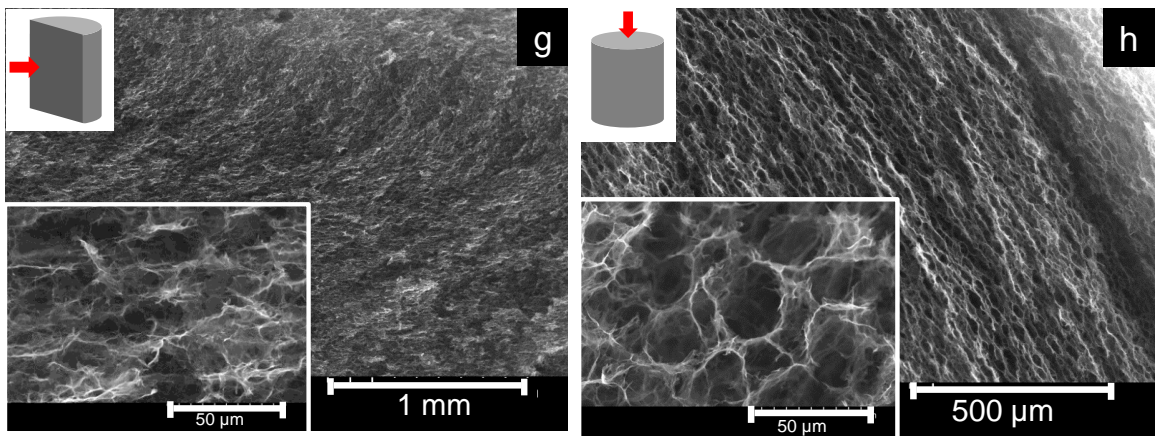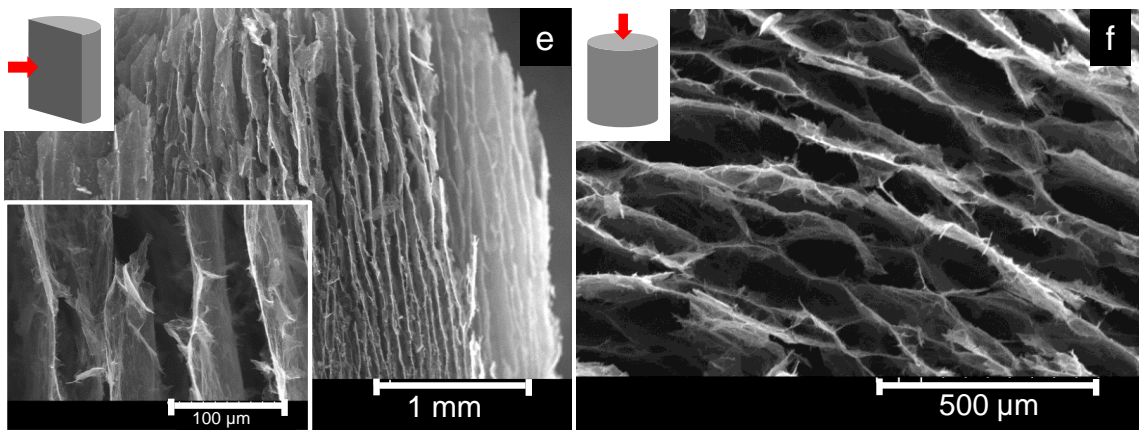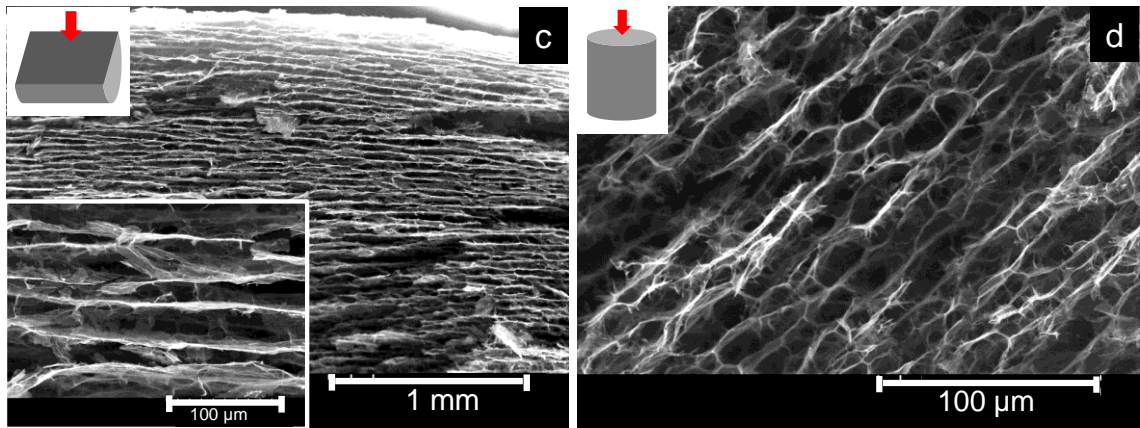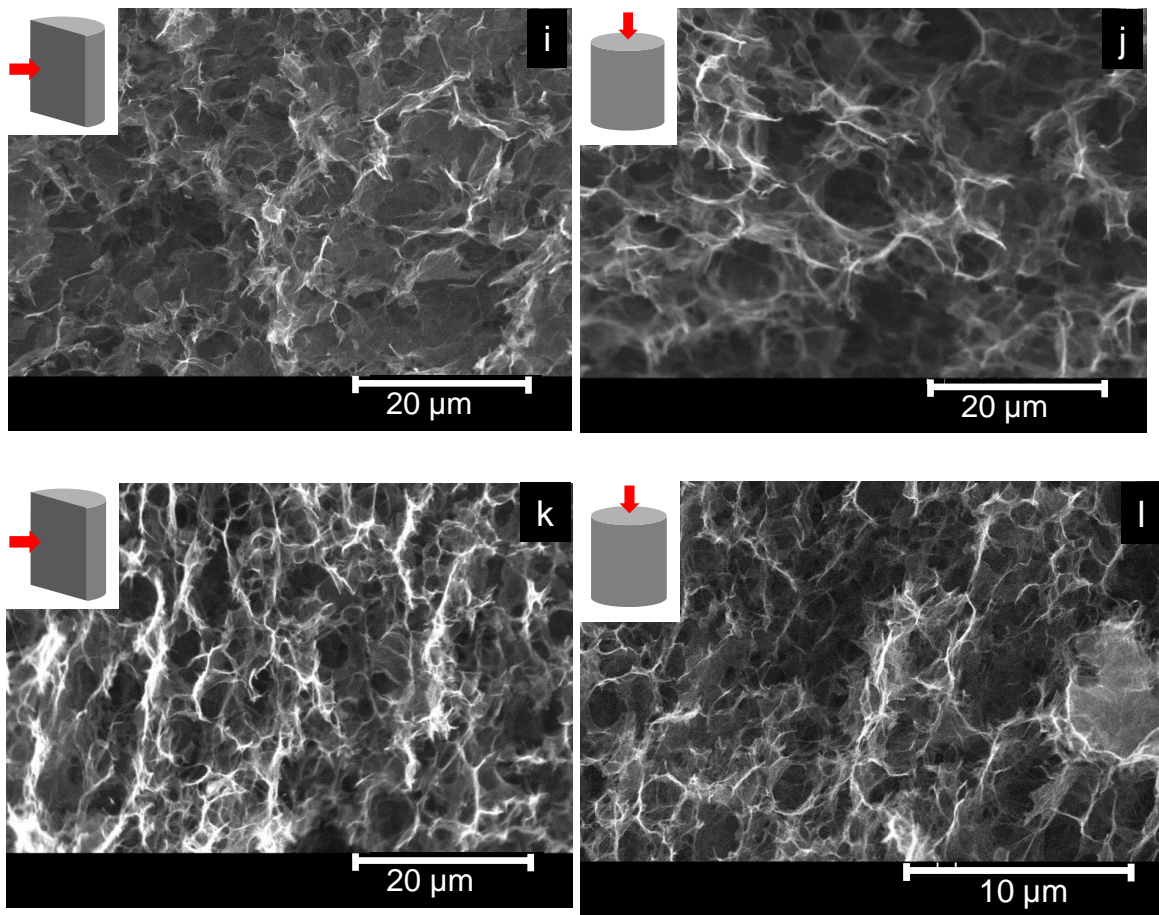
Figure 3. Representative SEM images of longitudinal sections (a,c,e,g,i, k) and cross sections (b,d,f,h,j,l) of aerogels prepared using unidirectional freezing from hydrogels attained at different hydrothermal times: (a,b) GA30min_U; (c,d) GA45min_U; (e,f) GA75min_U, (g,h) GA105min_U; (i,j) GA210min_U ; (k,l) GA18h_U.
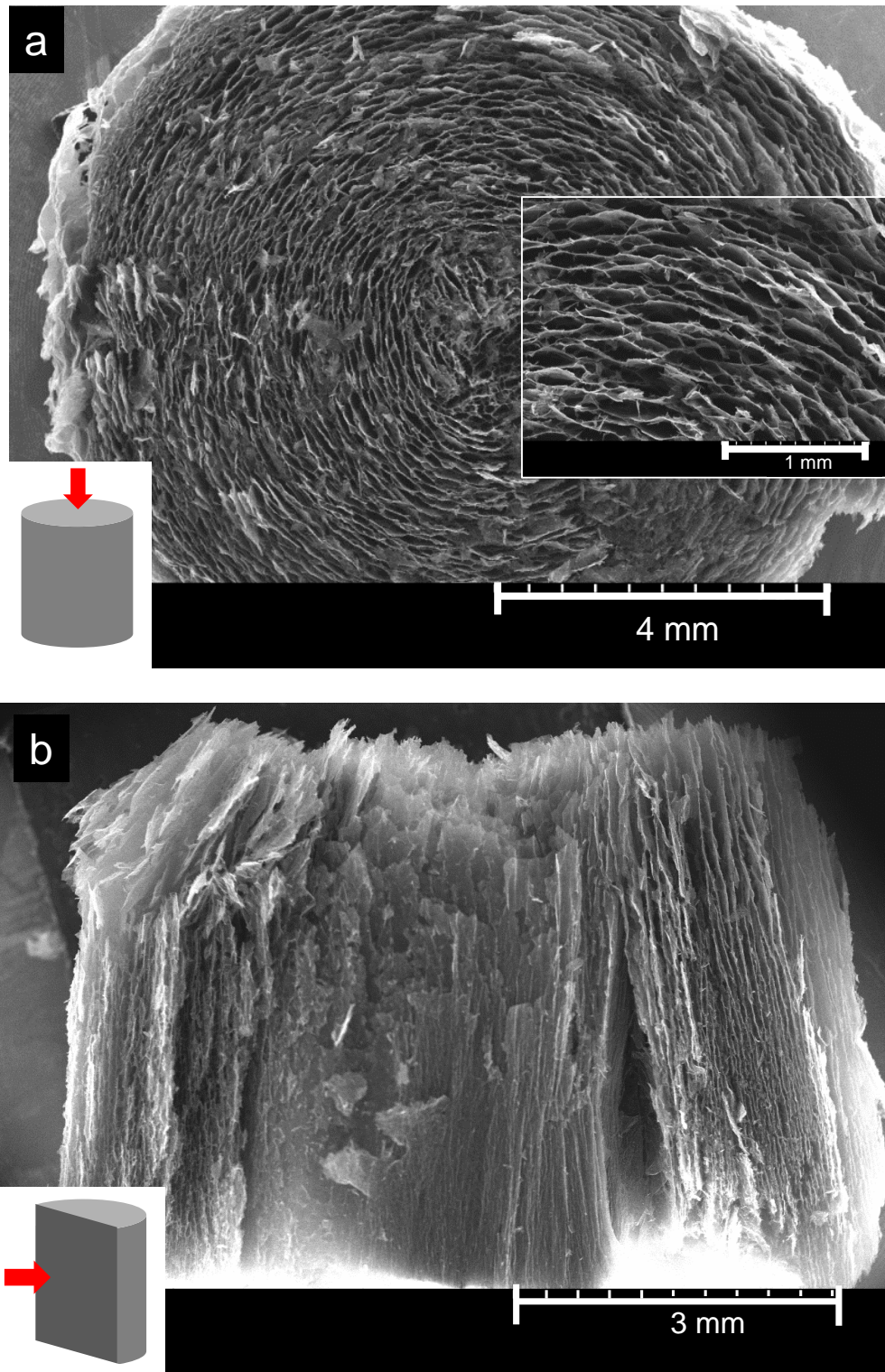
Figure 4. Low magnification SEM image of GA75min_U dried after unidirectional freezing: (a) cross-section, (b) longitudinal section
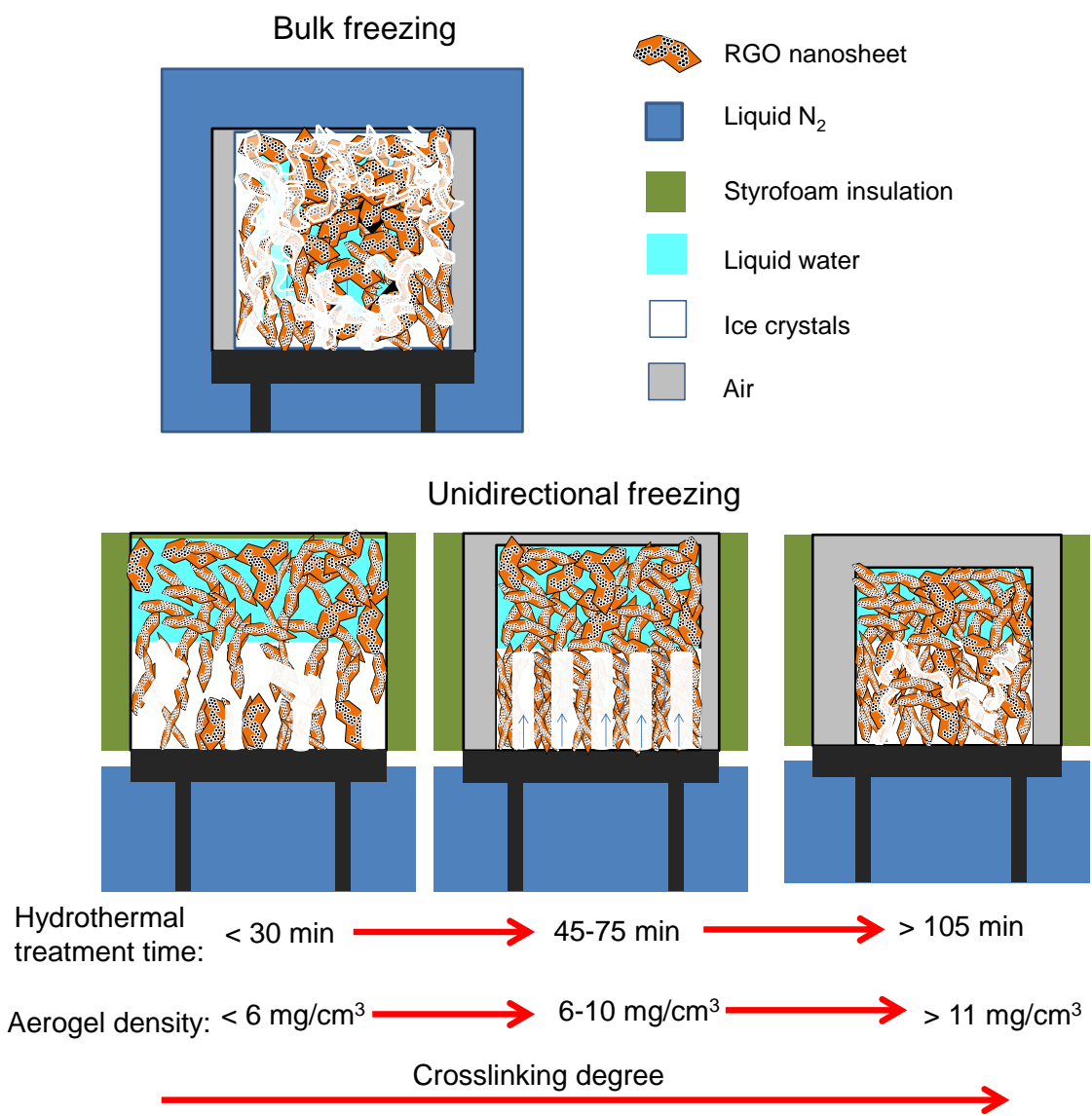
Scheme 2. Illustration of ice-crystal growth for the different freezing conditions used herein.

Scheme 2 illustrates a model for the ice crystal growth leading to the different morphologies of the aerogels found herein. This model can be generalized to hydrogels prepared by other reduction methods and starting from GO with different reduction degrees. Bulk freezing led to isotropic growth of the crystals while unidirectional freezing led to anisotropic crystal growth. Moreover, the morphology of the microchannels depends on the time of hydrothermal treatment and hence the

crosslinking degree. For times shorter than 30 min, *i.e.* before the hydrogel formation, certain orientation of the nanosheets takes place but the ice-crystal bars are interconnected horizontally, eventually leading upon drying to powdered samples and the absence of continuous microchannels as it happens for unidirectional freeze drying of GO colloids in the literature. The reasons are that the concentration of nanosheets is relatively low containing abundant water and the nanosheets are not still sufficiently crosslinked. In the hydrothermal treatment time span of 45-75 min, isolated ice bars grow from the bottom to top and they are enveloped by rGO nanosheets. These graphene nanosheets are crosslinked to a certain degree that is not so rigid to hinder their freedom to re-orient. The minimum diameter of ice crystals is about 25 μm. In contrast, for hydrogels prepared after hydrothermal treatments longer than 105 min, the ice-crystals cannot grow straight but winding. The reason is that they have to strive to find their way through a dense and rigid network of highly crosslinked graphene nanosheets and narrow pores. The openings in this case are smaller than 20 μm.

The optimized aerogel herein shows the most aligned and continuous microchannels among similar systems reported in the literature.[59-60, 65-66] This could be due to the fact that these studies used fixed conditions for the formation of rGO hydrogel and did not undertake a systematic optimization of the density (crosslinking degree) of hydrogel as in our work. Some of the few continuous microchannelled graphene aerogels in the literature started from GO dispersions reduced with a mild reductant (ascorbic acid) and heating.[32, 63-64] They found an optimum O/C ratio of 34% where the partially reduced GO sheets contain an optimum surface charge so that they remain mobile during formation of ice crystals. These rGO aerogels need a further thermal reduction to become graphene aerogels. Here we demonstrated that the nanosheets can be mobile for higher reduction extents such as ~14.4 % O/C ratio (Table 1). Therefore, our

experimental methodology proves to be superior to the pool of similar approaches since we advantageously apply hydrothermal treatments to reduce GO and crosslink rGO nanosheets in a single step without any reductant, saving time and avoiding post-synthesis reducing steps.

The degree of crosslinking between the nanosheets is affected by the surface chemistry , and physical changes such as removal of entrapped water, and van der Waals attractions, which changes as the hydrothermal treatment proceeds. Hence our approach relies on a precise control over this feature by the time of hydrothermal treatment, making the unidirectional freezing only effective within an accurate time, which provides great versatility. This contrasts to other similar works in the literature that achieve highly aligned microchannels but dealing with the manipulation of the sample during freezing rather, which may not be so controllable.[63]

To gain insight into the surface chemistry evolution, we characterised the aerogels prepared after different times of hydrothermal treatment by XPS and XRD (detailed experimental information in supplementary material). All the characterisation techniques indicated that there is a threshold in surface chemistry between 30 min and 45 min of hydrothermal treatment, whereby the hydrogel is formed. The oxygen content is reduced by half (Table 1). The fitting of the O1s and C1s peaks is shown in Figure S6 and the assignment of deconvoluted peaks has been carried out according to the literature[75-76] and explained in supporting information. The fitting of XPS O 1s reveals that the peak at 532.6±0.1 eV (O#3) ascribed to epoxide and ether decays dramatically in this time span. XRD reveals that beyond 30 min, the (001) peak at 2θ=10º found in GO becomes a shoulder and the (002) peak at 25.1º, as that found in graphite, emerges (Figure S7 of supporting information). After 45 min time, the oxygen content decreases only marginally. Thus, it is expected that beyond 45 min of hydrothermal treatment, the

hydrophobic interactions or π-π stacking of aromatic domains and the removal of entrapped water are the prevalent effects that increase crosslinking between graphene nanosheets.

In previous works[46, 77], it was demonstrated that aerogels are highly selective to the absorption of organics *vs.* polar solvents, with a high gravimetric absorption capacity and cyclic stability. The aerogels prepared by unidirectional and bulk freezing were compared in the absorption of hexane (Figure 5). The aerogels were used directly after freeze drying without any reduction posttreatment. An additional thermal postreatment at 1000º C in inert atmosphere, although decreases the O/C ratio from 13 to 1.7 % (Table S1), does not supply higher absorption capacity. It was found that aerogels with unidirectional channels (GA45min_U and GA75min_U) outperformed their random pore counterparts. For aerogels prepared using longer hydrothermal treatments (210 min and 18 h), in which the microchannels were not clearly observed by SEM, unidirectional freezing or bulk freezing does not provide significant differences in terms of absorption capacity.
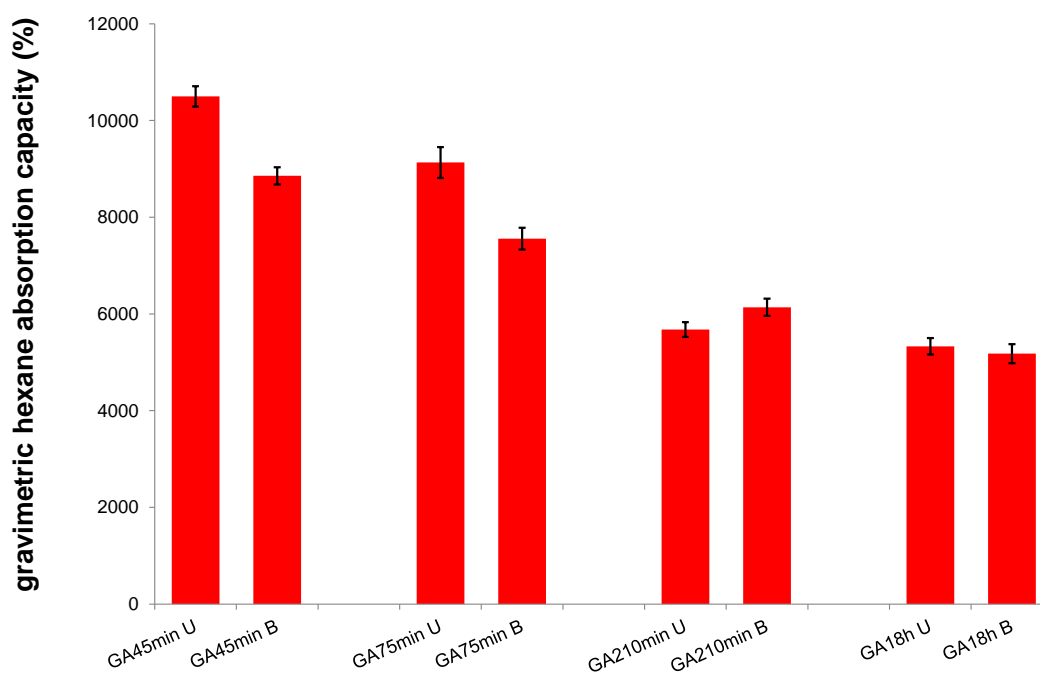
Figure 5. gravimetric absorption capacity of n-hexane for aerogels prepared with unidirectional freezing (U) and bulk freezing (B) for different hydrothermal treatment times. The values in the y-axis have been calculated as (W-Wo)/Wo x 100, where W is the weight after absorption and Wo is the intial weight of the aerogel.

For practical application in absorption the mechanical properties and the reusability of the absorbent are important parameters. Both aspects were demonstrated in our previous article for non-optimized porous structures.[46] That article included a movie showing the excellent and reversible compression properties of our aerogels. The tests of reusability revealed that the aerogels prepared for hydrothermal treatment times longer than 45 min do not lose absorption capacity for at least 20 cycles.

Besides the observed absorption behaviour of non-polar solvent in batch operation, the aerogel is also able to selectively adsorb an aromatic compound dissolved in an alkane. This adsorption was performed in continuous using the microfluidic set-up shown in Figure S2. In these experiments, a dye (Sudan III) was diluted in n-hexane and fed via a syringe, flowing through the aerogel. Sudan III is a neutral dye of composition related to azobenzene (Figure S3 top panel). It is lipophilic and it is adsorbed on the graphene sheets of the aerogels, most probably due to π- π stacking with the basal planes of graphene nanosheets. Panel a of Figure 6 depicts the representative adsorption breakthrough curves for the aerogels with unidirectional pores and for those with random pores. At the beginning of the experiment under continuous flow, the hexane at the outlet is colourless indicating total absorption of the dye and, after a certain time, a light red colour appears indicating the saturation of the aerogel adsorption sites. The onset of Sudan III occurs later and the curve is less steep for aerogel of unidirectional

pores compared to its random pore counterpart. The area above the curve, which indicates the amount of adsorbed Sudan III, was quantified for three repeated tests with different aerogels samples (Figure 6b). The quantity of adsorbed dye is systematically larger for aerogels with unidirectional pores. Both materials have the same chemical composition and weight and the small differences in BET Surface area cannot explain the differences in adsorption capacity. The only difference is the way they have been frozen, leading to different porous structures. Therefore, the amount of Sudan III adsorbed could be an indication of the surface of graphene exposed to the flow. Accordingly, the aerogel composed of unidirectional pores exposed a larger surface area to the flow. A plausible explanation could be that the foam-like aerogel exhibits a random pore structure with a wider pore size distribution and high tortuosity that may favour preferential paths, having some stagnant liquid in the pores. In contrast, for the aerogel of unidirectional pores, the flow pattern is more uniform throughout all the graphene aerogel pore volume thanks to the low tortuosity and more ordered structure of regular pores.
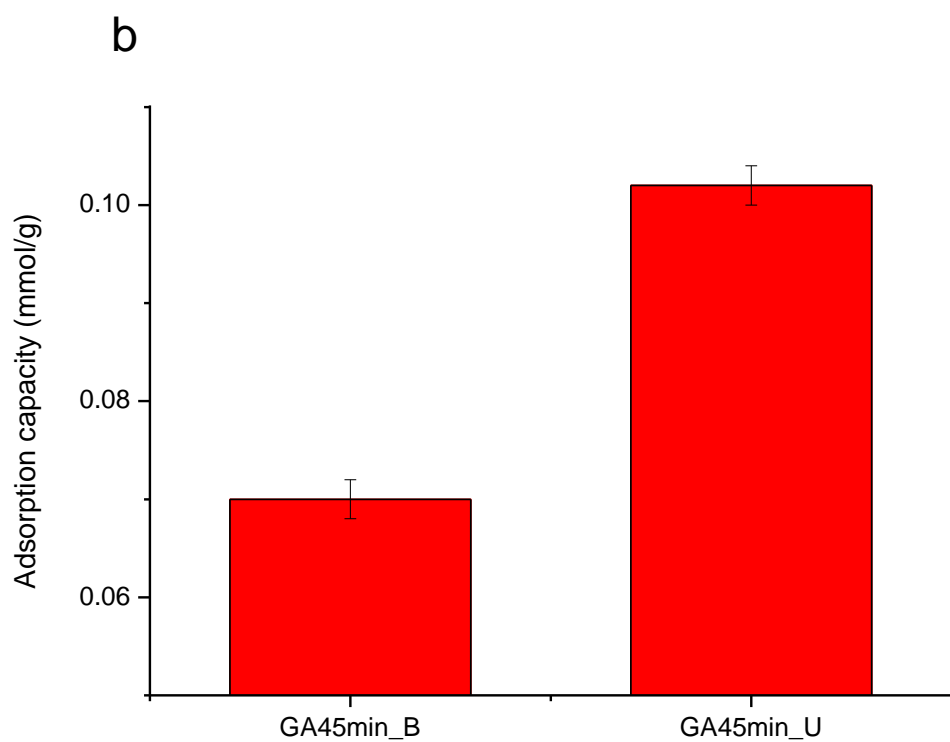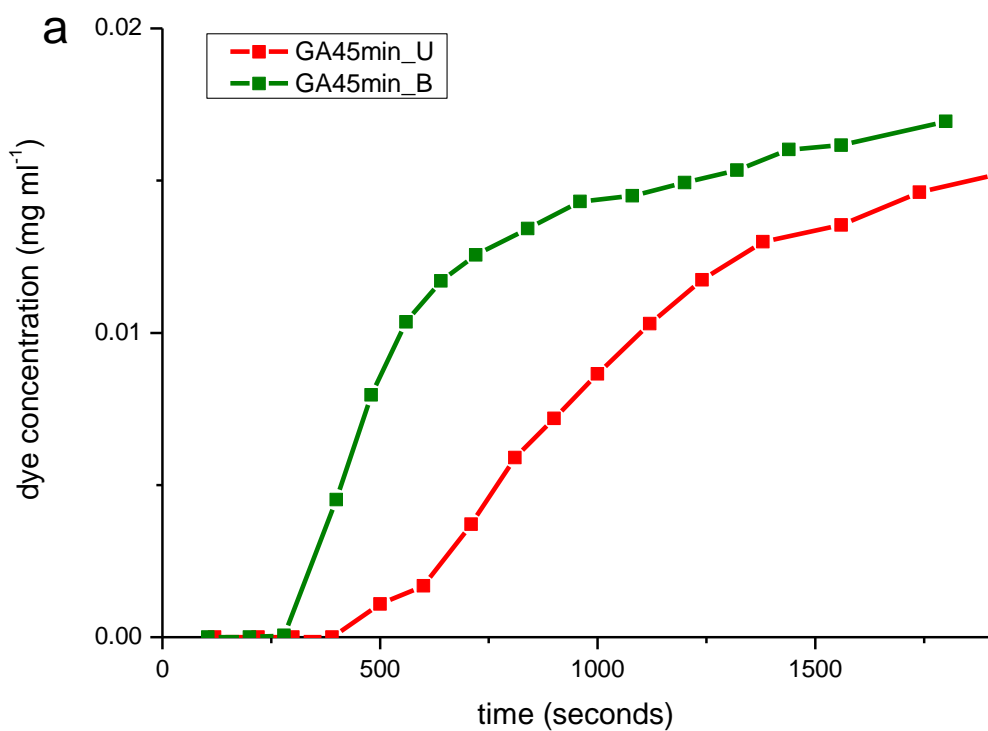
Figure 6. Adsorption of dye (Sudan III) in continuous flow (1 ml min^{-1} of 0.02 mg/ml of Sudan III in n-hexane) using aerogels with unidirectional oriented pores

(GA45min_U) and randomly oriented pores (GA45min_B): (a) representative breakthrough curves, (b) Adsorption capacity with error bars for three repeated tests.

Conclusions

Herein, unidirectional freeze casting technique is applied to rGO hydrogels prepared by hydrothermal reduction of GO aqueous dispersions in autoclave. This approach led to graphene aerogel monoliths exhibiting one of the most anisotropic and continuous microchannel structure among similar systems known to the best of our knowledge. Moreover, this approach avoids the subsequent reduction step that is commonly required for aerogels prepared by freeze drying of GO dispersions. It was disclosed that a certain degree of crosslinking, which is accurately controlled by the hydrothermal treatment time, is essential for the achievement of straight and continuous microchannels. When using hydrogels with an intermediate degree of crosslinking, *i.e.* those synthetized for the narrow time-span of 45-75 min of hydrothermal treatment, well-aligned and continuous microchannels are formed leading to honeycomb-like aerogels. In contrast, freeze drying is not effective to form the honeycomb structure for hydrogels with higher or lower degree of crosslinking. The effect of the crosslinking degree can be generalized to explain the different microstructures attained in the literature for GA synthetised using unidirectional freeze casting of initial GO with different reduction degrees or even with crosslinking additives.As a proof of concept, the aerogels with aligned pores have demonstrated several competitive advantages over their counterpart of randomly oriented pores. They provide ~20% higher gravimetric absorption capacity of non-polar solvent in batch operation and ~30% higher adsorption capacity of aromatic compounds in continuous microfluidic device. Besides of the

advantages demonstrated here, the anisotropic aerogels with aligned pores have excellent prospects for other applications such as biomedical engineering or energy storage, which are currently underway.

Acknowledgements

References

1.   Hu, H.; Zhao, Z.; Wan, W.; Gogotsi, Y.; Qiu, J., Ultralight and Highly Compressible Graphene Aerogels. *Adv. Mater.* **2013,** *25* (15), 2219-2223.
2.   Li, J.; Li, J.; Meng, H.; Xie, S.; Zhang, B.; Li, L.; Ma, H.; Zhang, J.; Yu, M., Ultra-light, Compressible and Fire-resistant Graphene Aerogel as a Highly Efficient and Recyclable Absorbent for Organic Liquids. *J. Mater. Chem. A* **2014,** *2* (9), 2934-2941.
3.   Qiu, L.; Zhang, X.; Yang, W.; Wang, Y.; Simon, G. P.; Li, D., Controllable Corrugation of Chemically Converted Graphene Sheets in Water and Potential Application for Nanofiltration. *Chem. Comm.* **2011,** *47* (20), 5810-5812.
4.   Hong, J.-Y.; Yun, S.; Wie, J. J.; Zhang, X.; Dresselhaus, M. S.; Kong, J.; Park, H. S., Cartilage-inspired Superelastic Ultradurable Graphene Aerogels Prepared by the Selective Gluing of Intersheet Joints. *Nanoscale* **2016,** *8* (26), 12900-12909.
5.   Wu, Y.; Yi, N.; Huang, L.; Zhang, T.; Fang, S.; Chang, H.; Li, N.; Oh, J.; Lee, J. A.; Kozlov, M.; Chipara, A. C.; Terrones, H.; Xiao, P.; Long, G.; Huang, Y.; Zhang, F.; Zhang, L.; Lepró, X.; Haines, C.; Lima, M. D.; Lopez, N. P.; Rajukumar, L. P.; Elias, A. L.; Feng, S.; Kim, S. J.; Narayanan, N. T.; Ajayan, P. M.; Terrones, M.; Aliev, A.; Chu, P.; Zhang, Z.; Baughman, R. H.; Chen, Y., Three-dimensionally Bonded Spongy Graphene Material with Super Compressive Elasticity and Near-zero Poisson's Ratio. *Natur. Comm.* **2015,** *6,* 6141.
6.   Worsley, M. A.; Pauzauskie, P. J.; Olson, T. Y.; Biener, J.; Satcher, J. H.; Baumann, T. F., Synthesis of Graphene Aerogel with High Electrical Conductivity. *J. Amer. Chem. Soc.* **2010,** *132* (40), 14067-14069.
7.   Worsley, M. A.; Pham, T. T.; Yan, A.; Shin, S. J.; Lee, J. R. I.; Bagge-Hansen, M.; Mickelson, W.; Zettl, A., Synthesis and Characterization of Highly Crystalline Graphene Aerogels. *ACS Nano* **2014,** *8* (10), 11013-11022.
8.   Xu, Z.; Zhang, Y.; Li, P.; Gao, C., Strong, Conductive, Lightweight, Neat Graphene Aerogel Fibers with Aligned Pores. *ACS Nano* **2012,** *6* (8), 7103-7113.

9. Cheng, Y.; Zhou, S.; Hu, P.; Zhao, G.; Li, Y.; Zhang, X.; Han, W., Enhanced Mechanical, Thermal, and Electric Properties of Graphene Aerogels via Supercritical Ethanol Drying and High-temperature Thermal Reduction. *Sci. Rep.* **2017,** *7* (1), 1439.

10. Andjelkovic, I.; Tran, D. N. H.; Kabiri, S.; Azari, S.; Markovic, M.; Losic, D., Graphene Aerogels Decorated with α-FeOOH Nanoparticles for Efficient Adsorption of Arsenic from Contaminated Waters. *ACS Appl. Mater. Interfaces* **2015,** *7* (18), 9758-9766.

11. Chen, W.; Li, S.; Chen, C.; Yan, L., Self-Assembly and Embedding of Nanoparticles by In Situ Reduced Graphene for Preparation of a 3D Graphene/Nanoparticle Aerogel. *Adv. Mater.* **2011,** *23* (47), 5679-5683.

12. De Marco, M.; Menzel, R.; Bawaked, S. M.; Mokhtar, M.; Obaid, A. Y.; Basahel, S. N.; Shaffer, M. S. P., Hybrid effects in graphene oxide/carbon nanotube-supported layered double hydroxides: enhancing the CO2 sorption properties. *Carbon* **2017,** *123*, 616-627.

13. Estevez, L.; Kelarakis, A.; Gong, Q.; Da'as, E. H.; Giannelis, E. P., Multifunctional Graphene/Platinum/Nafion Hybrids via Ice Templating. *J. Am. Chem. Soc.* **2011,** *133* (16), 6122-6125.

14. Fan, L.; Li, X.; Song, X.; Hu, N.; Xiong, D.; Koo, A.; Sun, X., Promising Dual-Doped Graphene Aerogel/SnS2 Nanocrystal Building High Performance Sodium Ion Batteries. *ACS Appl. Mater. Interfaces* **2018,** *10* (3), 2637-2648.

15. Jiang, Y.; Cheng, J.; Zou, L.; Li, X.; Huang, Y.; Jia, L.; Chi, B.; Pu, J.; Li, J., Graphene Foam Decorated with Ceria Microspheres as a Flexible Cathode for Foldable Lithium-Air Batteries. *ChemCatChem* **2017,** *9* (22), 4231-4237.

16. Lee, W. S. V.; Peng, E.; Choy, D. C.; Xue, J. M., Mechanically robust glucose strutted graphene aerogel paper as a flexible electrode. *J. Mater. Chem. A* **2015,** *3* (37), 19144-19147.

17. Li, L.; Li, B.; Zhang, J., Dopamine-mediated fabrication of ultralight graphene aerogels with low volume shrinkage. *J. Mater. Chem. A* **2016,** *4* (2), 512-518.

18. Liu, X.; Li, J.; Sun, J.; Zhang, X., 3D Fe3O4 nanoparticle/graphene aerogel for NO2 sensing at room temperature. *RSC Adv.* **2015,** *5* (90), 73699-73704.

19. Long, H.; Harley-Trochimczyk, A.; Pham, T.; Tang, Z.; Shi, T.; Zettl, A.; Carraro, C.; Worsley, M. A.; Maboudian, R., High Surface Area MoS2/Graphene Hybrid Aerogel for Ultrasensitive NO2 Detection. *Adv. Funct. Mater.* **2016,** *26* (28), 5158-5165.

20. Scaffaro, R.; Maio, A.; Lopresti, F.; Giallombardo, D.; Botta, L.; Bondì, M. L.; Agnello, S., Synthesis and self-assembly of a PEGylated-graphene aerogel. *Compos. Sci. Technol.* **2016,** *128*, 193-200.

21. Xu, H.; Wang, D.; Zhang, W.; Zhu, J.; Zhang, T.; Guo, X.; Zhang, Y.; Sun, Z.; Chen, J., SnO2 nanorods encapsulated within a 3D interconnected graphene network architecture as high-performance lithium-ion battery anodes. *Sustainable Energy Fuels* **2018,** *2* (1), 262-270.

22. Yilmaz, G.; Lu, X.; Ho, G. W., Cross-linker mediated formation of sulfur-functionalized V2O5/graphene aerogels and their enhanced pseudocapacitive performance. *Nanoscale* **2017,** *9* (2), 802-811.

23. Zhao, Y.; Xie, X.; Zhang, J.; Liu, H.; Ahn, H. J.; Sun, K.; Wang, G., MoS2 Nanosheets Supported on 3D Graphene Aerogel as a Highly Efficient Catalyst for Hydrogen Evolution. *Chem. – Eur. J.* **2015,** *21* (45), 15908-15913.

24. Guo, J.; Zhang, T.; Hu, C.; Fu, L., A three-dimensional nitrogen-doped graphene structure: a highly efficient carrier of enzymes for biosensors. *Nanoscale* **2015,** *7* (4), 1290-1295.

25.   Yang, X.; Zhuang, X.; Huang, Y.; Jiang, J.; Tian, H.; Wu, D.; Zhang, F.; Mai, Y.; Feng, X., Nitrogen-enriched hierarchically porous carbon materials fabricated by graphene aerogel templated Schiff-base chemistry for high performance electrochemical capacitors. *Polym. Chem.* **2015,** *6* (7), 1088-1095.

26.   Song, X.; Chen, Y.; Rong, M.; Xie, Z.; Zhao, T.; Wang, Y.; Chen, X.; Wolfbeis, O. S., A Phytic Acid Induced Super-Amphiphilic Multifunctional 3D Graphene-Based Foam. *Angew. Chem., Int. Ed.* **2016,** *55* (12), 3936-3941.

27.   Xie, B.; Ren, X.; Yan, X.; Dai, Z.; Hou, W.; Du, N.; Li, H.; Zhang, R., Fabrication of pore-rich nitrogen-doped graphene aerogel. *RSC Adv.* **2016,** *6* (27), 23012-23015.

28.   Zhou, Y.; Yen, C. H.; Fu, S.; Yang, G.; Zhu, C.; Du, D.; Wo, P. C.; Cheng, X.; Yang, J.; Wai, C. M.; Lin, Y., One-pot synthesis of B-doped three-dimensional reduced graphene oxide via supercritical fluid for oxygen reduction reaction. *Green Chem.* **2015,** *17* (6), 3552-3560.

29.   Zhao, X.; Li, M.; Dong, H.; Liu, Y.; Hu, H.; Cai, Y.; Liang, Y.; Xiao, Y.; Zheng, M., Interconnected 3 D Network of Graphene-Oxide Nanosheets Decorated with Carbon Dots for High-Performance Supercapacitors. *ChemSusChem* **2017,** *10* (12), 2626-2634.

30.   Wilson, E.; Islam, M. F., Ultracompressible, High-Rate Supercapacitors from Graphene-Coated Carbon Nanotube Aerogels. *ACS Appl. Mater. Interfaces* **2015,** *7* (9), 5612-5618.

31.   Enterría, M.; Martín-Jimeno, F. J.; Suárez-García, F.; Paredes, J. I.; Pereira, M. F. R.; Martins, J. I.; Martínez-Alonso, A.; Tascón, J. M. D.; Figueiredo, J. L., Effect of nanostructure on the supercapacitor performance of activated carbon xerogels obtained from hydrothermally carbonized glucose-graphene oxide hybrids. *Carbon* **2016,** *105*, 474-483.

32.   Petersen, S. V.; Qiu, L.; Li, D., Controlled Gelation of Graphene Towards Unprecedented Superstructures. *Chem. – Eur. J.* **2017,** *23* (54), 13264-13269.

33.   Barg, S.; Perez, F. M.; Ni, N.; do Vale Pereira, P.; Maher, R. C.; Garcia-Tuñon, E.; Eslava, S.; Agnoli, S.; Mattevi, C.; Saiz, E., Mesoscale assembly of chemically modified graphene into complex cellular networks. *Nat. Commun.* **2014,** *5*, 4328.

34.   Garg, R.; Rastogi, S. K.; Lamparski, M.; de la Barrera, S. C.; Pace, G. T.; Nuhfer, N. T.; Hunt, B. M.; Meunier, V.; Cohen-Karni, T., Nanowire-Mesh-Templated Growth of Out-of-Plane Three-Dimensional Fuzzy Graphene. *ACS Nano* **2017,** *11* (6), 6301-6311.

35.   Chua, C. K.; Pumera, M., The reduction of graphene oxide with hydrazine: elucidating its reductive capability based on a reaction-model approach. *Chem. Commun.* **2016,** *52* (1), 72-75.

36.   Dimiev, A. M.; Alemany, L. B.; Tour, J. M., Graphene Oxide. Origin of Acidity, Its Instability in Water, and a New Dynamic Structural Model. *ACS Nano* **2013,** *7* (1), 576-588.

37.   Rourke, J. P.; Pandey, P. A.; Moore, J. J.; Bates, M.; Kinloch, I. A.; Young, R. J.; Wilson, N. R., The Real Graphene Oxide Revealed: Stripping the Oxidative Debris from the Graphene-like Sheets. *Angew. Chem., Int. Ed.* **2011,** *50* (14), 3173-3177.

38.   Nuñez, J. D.; Benito, A. M.; Rouziere, S.; Launois, P.; Arenal, R.; Ajayan, P. M.; Maser, W. K., Graphene oxide-carbon nanotube hybrid assemblies: cooperatively strengthened OH[three dots, centered]O[double bond, length as m-dash]C hydrogen bonds and the removal of chemisorbed water. *Chem. Sci.* **2017,** *8* (7), 4987-4995.

39.   Yu, R.; Shi, Y.; Yang, D.; Liu, Y.; Qu, J.; Yu, Z.-Z., Graphene Oxide/Chitosan Aerogel Microspheres with Honeycomb-Cobweb and Radially Oriented Microchannel

Structures for Broad-Spectrum and Rapid Adsorption of Water Contaminants. *ACS Applied Materials & Interfaces* **2017,** *9* (26), 21809-21819.

40. Zhu, C.; Han, T. Y.-J.; Duoss, E. B.; Golobic, A. M.; Kuntz, J. D.; Spadaccini, C. M.; Worsley, M. A., Highly compressible 3D periodic graphene aerogel microlattices. *Nat. Commun.* **2015,** *6*, 6962.

41. Zhang, H.; Hussain, I.; Brust, M.; Butler, M. F.; Rannard, S. P.; Cooper, A. I., Aligned two- and three-dimensional structures by directional freezing of polymers and nanoparticles. *Nat. Mater.* **2005,** *4*, 787.

42. Nardecchia, S.; Carriazo, D.; Ferrer, M. L.; Gutierrez, M. C.; del Monte, F., Three dimensional macroporous architectures and aerogels built of carbon nanotubes and/or graphene: synthesis and applications. *Chem. Soc. Rev.* **2013,** *42* (2), 794-830.

43. Liu, P.; Cottrill, A. L.; Kozawa, D.; Koman, V. B.; Parviz, D.; Liu, A. T.; Yang, J.; Tran, T. Q.; Wong, M. H.; Wang, S.; Strano, M. S., Emerging trends in 2D nanotechnology that are redefining our understanding of "Nanocomposites". *Nano Today* **2018,** *21*, 18-40.

44. Wang, Z.; Shen, X.; Han, N. M.; Liu, X.; Wu, Y.; Ye, W.; Kim, J.-K., Ultralow Electrical Percolation in Graphene Aerogel/Epoxy Composites. *Chem. Mater.* **2016,** *28* (18), 6731-6741.

45. Anbari, A.; Chien, H.-T.; Datta, S. S.; Deng, W.; Weitz, D. A.; Fan, J., Microfluidic Model Porous Media: Fabrication and Applications. *Small 14* (18), 1703575.

46. Garcia-Bordeje, E.; Victor-Roman, S.; Sanahuja-Parejo, O.; Benito, A. M.; Maser, W. K., Control of the microstructure and surface chemistry of graphene aerogels via pH and time manipulation by a hydrothermal method. *Nanoscale* **2018,** *10* (7), 3526-3539.

47. Zhao, J.; Ren, W.; Cheng, H.-M., Graphene sponge for efficient and repeatable adsorption and desorption of water contaminations. *J. Mater. Chem. A* **2012,** *22* (38), 20197-20202.

48. Li, W. L.; Lu, K.; Walz, J. Y., Freeze casting of porous materials: review of critical factors in microstructure evolution. *Int. Mater. Rev.* **2012,** *57* (1), 37-60.

49. Gutiérrez, M. C.; Ferrer, M. L.; del Monte, F., Ice-Templated Materials: Sophisticated Structures Exhibiting Enhanced Functionalities Obtained after Unidirectional Freezing and Ice-Segregation-Induced Self-Assembly. *Chem. Mater.* **2008,** *20* (3), 634-648.

50. Wu, X.; Liu, Y.; Li, X.; Wen, P.; Zhang, Y.; Long, Y.; Wang, X.; Guo, Y.; Xing, F.; Gao, J., Preparation of Aligned Porous Gelatin Scaffolds by Unidirectional Freeze-drying Method. *Acta Biomater.* **2010,** *6* (3), 1167-1177.

51. Deville, S., Freeze-Casting of Porous Ceramics: A Review of Current Achievements and Issues. *Adv. Eng. Mater.* **2008,** *10* (3), 155-169.

52. Zou, J.; Liu, J.; Karakoti, A. S.; Kumar, A.; Joung, D.; Li, Q.; Khondaker, S. I.; Seal, S.; Zhai, L., Ultralight Multiwalled Carbon Nanotube Aerogel. *ACS Nano* **2010,** *4* (12), 7293-7302.

53. Gutiérrez, M. C.; Hortigüela, M. J.; Amarilla, J. M.; Jiménez, R.; Ferrer, M. L.; del Monte, F., Macroporous 3D Architectures of Self-Assembled MWCNT Surface Decorated with Pt Nanoparticles as Anodes for a Direct Methanol Fuel Cell. *J. Phys. Chem. C* **2007,** *111* (15), 5557-5560.

54. Vickery Jemma, L.; Patil Avinash, J.; Mann, S., Fabrication of Graphene–Polymer Nanocomposites With Higher-Order Three-Dimensional Architectures. *Adv. Mater.* **2009,** *21* (21), 2180-2184.

55.   Long, Y.; Zhang, C.; Wang, X.; Gao, J.; Wang, W.; Liu, Y., Oxidation of SO2 to SO3 catalyzed by graphene oxide foams. *J. Mater. Chem.* **2011,** *21* (36), 13934-13941.

56.   Wang, S.; Wang, Z.; Futamura, R.; Endo, M.; Kaneko, K., Highly microporous-graphene aerogel monolith of unidirectional honeycomb macro-textures. *Chem. Phys. Lett.* **2017,** *673*, 38-43.

57.   Han, N. M.; Wang, Z.; Shen, X.; Wu, Y.; Liu, X.; Zheng, Q.; Kim, T.-H.; Yang, J.; Kim, J.-K., Graphene Size-Dependent Multifunctional Properties of Unidirectional Graphene Aerogel/Epoxy Nanocomposites. *ACS Appl. Mater. Interfaces* **2018,** *10* (7), 6580-6592.

58.   Wang, S.; Tristan, F.; Minami, D.; Fujimori, T.; Cruz-Silva, R.; Terrones, M.; Takeuchi, K.; Teshima, K.; Rodríguez-Reinoso, F.; Endo, M.; Kaneko, K., Activation routes for high surface area graphene monoliths from graphene oxide colloids. *Carbon* **2014,** *76*, 220-231.

59.   He, Y.; Liu, Y.; Wu, T.; Ma, J.; Wang, X.; Gong, Q.; Kong, W.; Xing, F.; Liu, Y.; Gao, J., An environmentally friendly method for the fabrication of reduced graphene oxide foam with a super oil absorption capacity. *J. Hazard. Mater.* **2013,** *260*, 796-805.

60.   Kuang, J.; Liu, L.; Gao, Y.; Zhou, D.; Chen, Z.; Han, B.; Zhang, Z., A hierarchically structured graphene foam and its potential as a large-scale strain-gauge sensor. *Nanoscale* **2013,** *5* (24), 12171-12177.

61.   Zhang, N.; Qiu, H.; Si, Y.; Wang, W.; Gao, J., Fabrication of highly porous biodegradable monoliths strengthened by graphene oxide and their adsorption of metal ions. *Carbon* **2011,** *49* (3), 827-837.

62.   Zhang, P.; Li, J.; Lv, L.; Zhao, Y.; Qu, L., Vertically Aligned Graphene Sheets Membrane for Highly Efficient Solar Thermal Generation of Clean Water. *ACS Nano* **2017,** *11* (5), 5087-5093.

63.   Li, X.-H.; Liu, P.; Li, X.; An, F.; Min, P.; Liao, K.-N.; Yu, Z.-Z., Vertically aligned, ultralight and highly compressive all-graphitized graphene aerogels for highly thermally conductive polymer composites. *Carbon* **2018,** *140*, 624-633.

64.   Qiu, L.; Liu, J. Z.; Chang, S. L. Y.; Wu, Y.; Li, D., Biomimetic superelastic graphene-based cellular monoliths. *Nat. Commun.* **2012,** *3*, 1241.

65.   Li, X.-H.; Li, X.; Liao, K.-N.; Min, P.; Liu, T.; Dasari, A.; Yu, Z.-Z., Thermally Annealed Anisotropic Graphene Aerogels and Their Electrically Conductive Epoxy Composites with Excellent Electromagnetic Interference Shielding Efficiencies. *ACS Applied Materials & Interfaces* **2016,** *8* (48), 33230-33239.

66.   Liu, T.; Huang, M.; Li, X.; Wang, C.; Gui, C.-X.; Yu, Z.-Z., Highly compressible anisotropic graphene aerogels fabricated by directional freezing for efficient absorption of organic liquids. *Carbon* **2016,** *100*, 456-464.

67.   Liu, R.; Wan, L.; Liu, S.; Pan, L.; Wu, D.; Zhao, D., An Interface-Induced Co-Assembly Approach Towards Ordered Mesoporous Carbon/Graphene Aerogel for High-Performance Supercapacitors. *Adv. Funct. Mater.* **2015,** *25* (4), 526-533.

68.   Xu, Y.; Sheng, K.; Li, C.; Shi, G., Self-Assembled Graphene Hydrogel via a One-Step Hydrothermal Process. *ACS Nano* **2010,** *4* (7), 4324-4330.

69.   Rafiee, M. A.; Rafiee, J.; Wang, Z.; Song, H.; Yu, Z.-Z.; Koratkar, N., Enhanced Mechanical Properties of Nanocomposites at Low Graphene Content. *ACS Nano* **2009,** *3* (12), 3884-3890.

70.   Li, D.; Müller, M. B.; Gilje, S.; Kaner, R. B.; Wallace, G. G., Processable aqueous dispersions of graphene nanosheets. *Nat. Nanotechnol.* **2008,** *3*, 101.

71.   Lucchese, M. M.; Stavale, F.; Ferreira, E. H. M.; Vilani, C.; Moutinho, M. V. O.; Capaz, R. B.; Achete, C. A.; Jorio, A., Quantifying ion-induced defects and Raman relaxation length in graphene. *Carbon* **2010,** *48* (5), 1592-1597.

72.   Tuinstra, F.; Koenig, J. L., Raman Spectrum of Graphite. *The Journal of Chemical Physics* **1970,** *53* (3), 1126-1130.

73.   Shen, Y.; Zhang, H.-B.; Zhang, H.; Ren, W.; Dasari, A.; Tang, G.-S.; Yu, Z.-Z., Structural evolution of functionalized graphene sheets during solvothermal reduction. *Carbon* **2013,** *56*, 132-138.

74.   Stankovich, S.; Dikin, D. A.; Piner, R. D.; Kohlhaas, K. A.; Kleinhammes, A.; Jia, Y.; Wu, Y.; Nguyen, S. T.; Ruoff, R. S., Synthesis of graphene-based nanosheets via chemical reduction of exfoliated graphite oxide. *Carbon* **2007,** *45* (7), 1558-1565.

75.   Okpalugo, T. I. T.; Papakonstantinou, P.; Murphy, H.; McLaughlin, J.; Brown, N. M. D., High resolution XPS characterization of chemical functionalised MWCNTs and SWCNTs. *Carbon* **2005,** *43* (1), 153-161.

76.   Xia, W.; Wang, Y.; Bergsträßer, R.; Kundu, S.; Muhler, M., Surface characterization of oxygen-functionalized multi-walled carbon nanotubes by high-resolution X-ray photoelectron spectroscopy and temperature-programmed desorption. *Applied Surface Science* **2007,** *254* (1), 247-250.

77.   Wang, B.; Liang, W.; Guo, Z.; Liu, W., Biomimetic super-lyophobic and super-lyophilic materials applied for oil/water separation: a new strategy beyond nature. *Chem. Soc. Rev.* **2015,** *44* (1), 336-361.

Supporting Information Available: Set up used for adsorption experiments; UV-vis absorbance spectra of Sudan III; characterization of aerogels after heat treatment